Magnification of signatures of a topological phase transition by quantum zero point motion

Pedro L. e S. Lopes[1,*] and Pouyan Ghaemi[2]

[1]*Instituto de Física Gleb Wataghin, Universidade Estadual de Campinas, Campinas, São Paulo 13083-970, Brazil*
[2]*Department of Physics, City College of the City University of New York, New York, New York 10031, USA*

We show that the zero point motion of a vortex in superconducting doped topological insulators leads to significant changes in the electronic spectrum at the topological phase transition in this system. This topological phase transition is tuned by the doping level, and the corresponding effects are manifest in the density of states at energies which are on the order of the vortex fluctuation frequency. Although the electronic energy gap in the spectrum generated by a stationary vortex is but a small fraction of the bulk superconducting gap, the vortex fluctuation frequency may be much larger. As a result, this quantum zero point motion can induce a discontinuous change in the spectral features of the system at the topological vortex phase transition to energies which are well within the resolution of scanning tunneling microscopy. This discontinuous change is exclusive to superconducting systems in which we have a topological phase transition. Moreover, the phenomena studied in this paper present effects of Magnus forces on the vortex spectrum which are not present in the ordinary *s*-wave superconductors. Finally, we demonstrate explicitly that the vortex in this system is equivalent to a Kitaev chain. This allows for the mapping of the vortex fluctuating scenario in three dimensions into similar one-dimensional situations in which one may search for other novel signatures of topological phase transitions.

PACS number(s): 73.20.At, 74.25.Ha, 64.70.Tg

I. INTRODUCTION

Topologically distinct phases which cannot be classified by the classical Landau paradigm comprise some of the most recently discovered states of matter [1–3]. An important signature of these topological phases is the appearance of novel low-energy robust edge states; one such state is the so-called Majorana bound state at the edges of topological superconductors [4]. As ubiquitous signatures, the detection of these neutral fermions has been the main trend in the characterization of particle-hole symmetric topological phases. Although evidence of Majorana fermion physics has been identified in tunneling [5] and scanning tunneling microscopy (STM) measurements [6], the interpretation of their signatures is controversial in many cases as the imprints from the topological regime are often mixed with signals from disorder and extra undesired quasiparticles.

Whereas the aforementioned gapless edge states act as a signature of topologically nontrivial regimes, the signatures of the *transition* from a topologically trivial to a topological phase present themselves in the bulk by the closing and reopening of the excitation energy gap [7–9]. In many of the proposed systems which can be tuned through a topological phase transition (TPT), the excitation gap is very small compared with experimental resolutions and cannot be probed directly.

In this paper, we show that quantum fluctuations can *shift the spectral weight* in the density of states of a given system before and after a TPT to further separated energies and, as a result, magnify the change in the spectrum resulting from this process. This situation will be relevant as long as the sample's temperature is below $\hbar\omega_0/k_B$, where ω_0 is the pinning frequency and k_B is Boltzmann's constant. We discuss this effect in the context of the chemical potential induced topological phase transition in the vortices of superconducting

doped topological insulators (TIs). In this particular situation, we also demonstrate how the effects of Magnus forces on the vortex dynamics [10] have a novel signature in the spectral change at this TPT, exposing the pumping of vortex modes responsible for the phase transition as described below. Our results are general, however, and can be extended to other types of topological phase transitions. To demonstrate this, we present a way to map the three-dimensional (3D) situation into a one-dimensional (1D) setting in terms of wire networks which may be used to probe for the topological phase transition of actual Kitaev chains, Su-Schrieffer-Heeger (SSH) chains, and other unidimensional topological chains.

To understand how quantum fluctuations affect vortices in superconducting doped TIs we start by discussing vortex dynamics in regular superconductors (SCs). This physics has been widely studied [11,12] and, given the natural length scale of vortices, their different properties might display both classical and quantum phenomena. Within the BCS theory of superconductivity, a stationary vortex affects the spectrum of the superconductor by generating in-gap modes localized around and along the vortex core [13]. The energy of these discrete bound states, known as Caroli–de Gennes–Matricon (CdGM) modes, is given by $\epsilon_l = \frac{\Delta^2}{\mu}(l + \frac{1}{2})$ where Δ is the size of the bulk SC gap, μ is the Fermi energy, and l is an integer. The signatures of these in-gap states have been experimentally observed by STM measurements [14,15]. In practice, however, even though the spatial resolution of STM is well within the size of the vortex modes [16], given the small size of their so-called minigap $\delta \equiv \frac{\Delta^2}{\mu}$, the energy of each single mode is hard to be resolved, and usually multiple modes are observed together [14].

It is well known that the pinning of vortices is necessary for the stability of type-II SCs. The discussion above would be the final status of the problem for pinned vortices were they absolutely static. Although a pinned vortex has a fixed position at the sample, even at the lowest temperatures, its quantum zero point motion cannot be ignored. Interestingly, it was shown that

_____

*plslopes@ifi.unicamp.br

such quantum fluctuations affect the quasiparticle spectrum, moving part of the spectral weights of the in-gap vortex modes to the frequencies associated with vortex fluctuations [17–19]. We then contend that exploiting this ubiquitous quantum-mechanical phenomenon to probe for TPTs is a promising idea, leading to novel signatures of these transitions.

To test this approach, superconducting doped TIs arise as the most natural test ground. The discovery of superconductivity in doped TIs triggered several studies, particularly because of the suggestions that doped TIs might realize topological superconductivity [20–24]. Theoretical studies of superconductivity in the surface states of TIs started even before the experimental realization of bulk superconductivity in doped TIs when it was shown that, theoretically, if superconductivity is induced in their helical surface states, vortex modes will include a zero-energy Majorana bound state [25]. In the context of bulk superconducting doped TIs, it was later shown that the Majorana mode at the ends of a vortex line persist up to a critical value of doping in these systems as well [26–28]. At this critical doping level, the two Majorana modes at the ends of the vortex hybridize and become gapped. The presence or absence of Majorana modes at the end of the vortex line contrast the two topologically distinct phases. In fact, the vortex in doped superconducting TIs becomes effectively equivalent to a Kitaev chain, one of the pioneering theoretical models to realize topological phases and phase transitions with Majorana edge states [29] (check also Sec. V of the present paper).

As desired, the signature of this TPT also shows up in the spectrum of the states extended along the vortex. The original mechanism lies in the CdGM modes. The important property of these states is that they are gapped by the small energy scale of the mentioned minigap. This energy protects the surface Majorana zero modes, confining them to the surface of the sample. Because of strong spin-orbit coupling and the resulting band inversion of TIs [30], the Fermi surface here has nontrivial topological properties which show up as a nonzero Berry connection. The CdGM modes then inherit this Berry phase as a modification to their energy spectrum, which also separates in two sets due to the existence of two degenerate TI Fermi surfaces, which becomes $E_l^\pm = \frac{\Delta^2}{E_F}(l \mp \frac{1}{2} \pm \frac{\Phi_b(\mu)}{2\pi})$. Here Φ_b is the Berry phase around the curve on the Fermi surface defined by setting the wave vector along the vortex line equal to zero. In this case, when $\Phi_b = \pi$, $E_0^\pm = 0$ and the zero-energy surface Majorana modes at the ends of the vortex can merge through the gapless $l = 0$ mode which is now extended along the vortex. The richness introduced by spin-orbit coupling and topology in this system leads to the signatures that we demonstrate.

For the physical picture of a fluctuating vortex to be reasonable, its position and cross-sectional structure must be well defined. Testing with some real numbers, copper doped Bi$_2$Se$_3$ was the first topological insulator found to become superconducting upon doping at 3.8 K [20]. One must spatially resolve the local density of states (LDOS) at the vortex core which, as we demonstrate, comes from the $l = 0$ and $l = 1$ CdGM modes. Their maxima lie at $r = 0$ and are separated from the next closest mode (with $l = -1$) by the Fermi wave-vector scale $r = 1/k_F \approx 10$ Å, which is well within the resolution of STM. Regarding the energy scales, the change in spectrum at the TPT happens at the minigap energy scale of

$\delta \approx 5 \times 10^{-3}$ K. This is very small compared to the spectral resolution of STM, which is on the order of the measurement temperature $(3k_B T)$ [16]. It is then clear that an important obstacle to the verification of topological phase transitions in this system by STM is the small excitation gap. Overcoming this energy scale problem is the main role of the vortex position fluctuation we analyze.

The paper is organized as follows. In Sec. II we explain the model on which we base our calculations. In Sec. III we follow Ref. [17] showing how the vortex fluctuations induce a self-energy correction which redistributes the peak weights in the LDOS for our specific model. This affects directly the tunneling conductance measured in STM experiments, and in Sec. IV we demonstrate what are the novel consequences of this phenomenon for the vortex TPT in doped TIs. We believe that the approach we describe in the bulk of our paper is generalizable to other situations, and we dedicate Sec. V to stipulate how to translate the ideas from the 3D context to 1D situations concerning Kitaev chains or other linear or quasilinear topological phases. We conclude in Sec. VI. As computations are a bit involved, we avoid displaying them throughout our narrative as much as we can. We refer the reader to the appendices where details are displayed thoroughly whenever necessary.

II. FLUCTUATING VORTEX MODEL

Superconductivity and the vortex quantum phase transition (VQPT) in doped topological insulators may be understood in the weak pairing limit ($\xi k_F \gg 1$, where ξ is the SC coherence length) [26]. In this regime, a gradient expansion can be deployed to study the effects of the fluctuating vortex position in the low-energy spectrum [17].

We start with an action of the form $\mathcal{S} = \mathcal{S}_{\text{BdG}} + \mathcal{S}_{\text{eff}}^{\text{vortex}}$. The first term is a Bogoliubov–de Gennes (BdG) action for the superconducting doped TI,

$$\mathcal{S}_{\text{BdG}} = \frac{1}{2} \int d^2r \, d\tau \, \Psi^\dagger (\partial_\tau + H_{\text{BdG}}) \Psi, \qquad (1)$$

where

$$H_{\text{BdG}} = \begin{bmatrix} H_{\text{TI}} - \mu & \Delta[\mathbf{r} - \mathbf{R}(\tau)] \\ \Delta^\dagger[\mathbf{r} - \mathbf{R}(\tau)] & -H_{\text{TI}} + \mu \end{bmatrix}. \qquad (2)$$

Here μ is the chemical potential, and the effective low-energy 3D TI Hamiltonian is given by

$$H_{\text{TI}} = -i v_D \tau_x \mathbf{s} \cdot \nabla + \tau_z (m + \epsilon \nabla^2), \qquad (3)$$

with Nambu spinor $\Psi = (\psi, i s_y \psi^\dagger)^T$ and where $\psi = (\psi_{A\uparrow}, \psi_{A\downarrow}, \psi_{B\uparrow}, \psi_{B\downarrow})$. A, B are orbital indices, and τ_i and s_i Pauli matrices act on orbital and spin Hilbert spaces, respectively. The superconducting pairing $\Delta[\mathbf{r} - \mathbf{R}(\tau)]$ contains a vortex profile centered at a fluctuating position $\mathbf{R}(\tau)$ whose dynamics is governed by [17]

$$\mathcal{S}_{\text{eff}}^{\text{vortex}} = \frac{m_v}{2} \int \frac{d\omega}{2\pi} \mathbf{R}^\dagger(i\omega) \begin{pmatrix} \omega^2 + \omega_0^2 & \omega_c \omega \\ -\omega_c \omega & \omega^2 + \omega_0^2 \end{pmatrix} (i\omega). \qquad (4)$$

Physically, the action (4) describes a particle of mass m_v oscillating in a harmonic trap of frequency ω_0 which depends

on the properties of the trapping potential [17]. This oscillator frequency dictates the qualitative features of the energy peak distribution of the LDOS. Finally, ω_c corresponds to a Magnus force acting on the vortex. The frequency ω_c will be shown to play an essential role, introducing an energy scale for the chemical potential in which we have distinguished signatures of the VQPT in the system's LDOS.

To capture the coupling between electronic excitations and vortex fluctuations, we expand the superconducting pairing around the vortex rest position $\Delta[\mathbf{r} - \mathbf{R}(\tau)] \approx \Delta(\mathbf{r}) - \partial_{\mathbf{r}}\Delta(\mathbf{r}) \cdot \mathbf{R}(\tau)$. This approximation is valid at weak coupling [17], which is also the regime of validity of Hamiltonian (2). Within this formalism, the full problem is described by a perturbative action $\mathcal{S} = \mathcal{S}_0 + \mathcal{S}_{\text{eff}}^{\text{vortex}} + \mathcal{S}_{\text{int}}$. $\mathcal{S}_0$ is given by (1) with the BdG Hamiltonian in the stationary vortex limit $\mathbf{R}(\tau) = 0$ [explicitly given in (A1)]. The interaction term is given by

$$\mathcal{S}_{\text{int}} = -\int d^2r \, d\tau \, \mathbf{R}(\tau) \cdot \Psi^\dagger \begin{pmatrix} 0 & \partial_{\mathbf{r}}\Delta \\ \partial_{\mathbf{r}}\Delta^\dagger & 0 \end{pmatrix} \Psi. \quad (5)$$

The interaction between the vortex modes and the fluctuations in the vortex position leads to a self-energy correction to the energy of the CdGM modes.

III. PERTURBED LDOS

Assuming a singlet intraorbital pairing for doped TIs, the VQPT was found originally by an exact diagonalization of lattice toy models and a semiclassical study of the BdG mean-field Hamiltonian [26] as well as numerically solving the self-consistent BdG equations [28]. In order to study the effects of vortex fluctuations on the LDOS, it is convenient to use a basis which diagonalizes the Hamiltonian at the limit of a static vortex. Thus, we present the VQPT by a novel real-space diagonalization of the BdG equation of Hamiltonian (A1) following the ideas from Ref. [31]. The details follow in Appendix A. We expand the Grassmann fields in terms of eigenvectors of the static-vortex BdG Hamiltonian H_{BdG}^0 as $\Psi = \sum_{q=1}^8 \sum_{ln} \chi_{ln}^q(\mathbf{r}) \psi_{ln}^q(\tau)$. The eight arising bands obey $H_{\text{BdG}}^0 \chi_{ln}^q(\mathbf{r}) = E_{ln}^q \chi_{ln}^q(\mathbf{r})$ where l and n label conserved quantum numbers. Precisely, l represents a generalized angular momentum $\tilde{L}_z = -i\partial_\theta - \frac{s_z + \rho_z}{2}$ which commutes with the Hamiltonian (see Ref. [26] or Appendix A), whereas n labels the different eigenstates of the radial BdG equation at fixed l. At weak coupling, we further project into the two bands which cross the doubly degenerate Fermi surface of H_{TI}. Labeling these states by $\sigma \equiv \pm$, we have, at low energies, $\Psi \approx \sum_{ln} \chi_{ln}^+(\mathbf{r}) \psi_{ln}^+(\tau) + \chi_{ln}^-(\mathbf{r}) \psi_{ln}^-(\tau)$ with

$$\chi_{ln}^+(\mathbf{r}) = \frac{1}{\sqrt{2\pi}} \int dk \begin{pmatrix} \frac{c_{lk}^n}{\sqrt{\mathcal{N}_k^+}} \begin{pmatrix} e^{-i(l-1)\theta} k J_{l-1}(kr) \\ 0 \\ 0 \\ e^{-il\theta}\left(m_k - \sqrt{m_k^2 + k^2}\right) J_l(kr) \end{pmatrix} \\ \frac{d_{lk}^n}{\sqrt{\mathcal{N}_k^-}} \begin{pmatrix} e^{-il\theta}\left(m_k + \sqrt{m_k^2 + k^2}\right) J_l(kr) \\ 0 \\ 0 \\ k e^{-i(l+1)\theta} J_{l+1}(kr) \end{pmatrix} \end{pmatrix} = \begin{pmatrix} \mathbf{u}_{ln}^+(\mathbf{r}) \\ \mathbf{v}_{ln}^+(\mathbf{r}) \end{pmatrix}, \quad (6)$$

$$\chi_{ln}^-(\mathbf{r}) = \frac{1}{\sqrt{2\pi}} \int dk \begin{pmatrix} \frac{\bar{c}_{lk}^n}{\sqrt{\mathcal{N}_k^-}} \begin{pmatrix} 0 \\ e^{-il\theta}\left(m_k + \sqrt{m_k^2 + k^2}\right) J_l(kr) \\ e^{-i(l-1)\theta} k J_{l-1}(kr) \\ 0 \end{pmatrix} \\ \frac{\bar{d}_{lk}^n}{\sqrt{\mathcal{N}_k^+}} \begin{pmatrix} 0 \\ e^{-i(l+1)\theta} k J_{l+1}(kr) \\ e^{-il\theta}\left(m_k - \sqrt{m_k^2 + k^2}\right) J_l(kr) \\ 0 \end{pmatrix} \end{pmatrix} = \begin{pmatrix} \mathbf{u}_{ln}^-(\mathbf{r}) \\ \mathbf{v}_{ln}^-(\mathbf{r}) \end{pmatrix}. \quad (7)$$

The numerical diagonalization may be performed replacing the infinite system with a disk of finite radius R with a profile of $\Delta_0(r) = \Delta_0 \tanh(r/\xi)$ for the vortex and solving the secular equation for the Fourier-Bessel coefficients c_{lk}^n, d_{lk}^n, $\bar{c}_{lk}^n$, and $\bar{d}_{lk}^n$ (details follow in Appendix A and references therein).

To study the VQPT we consider the lowest-energy vortex modes. These are the CdGM modes and allow fixing the label $n \rightarrow n_{\text{CdGM}}$, which we drop. The two sectors (labeled by $\sigma = \pm$) are connected by a particle-hole (PH) conjugation $\mathcal{C} = \rho_y s_y \mathcal{K}$ operator ($\mathcal{K}$ is the complex conjugation operator) as $\mathcal{C}\chi_l^+ = \chi_{-l}^-$. The energies of the CdGM vortex modes in this case are the expected [26]

$$E_l^\pm = \frac{\Delta^2}{E_F}\left(l \mp \frac{1}{2} \pm \frac{\Phi_b(\mu)}{2\pi}\right), \quad (8)$$

so that $E_l^+ = -E_{-l}^-$. Here $\Phi_b(\mu)$ is the Berry phase calculated around the Fermi surface on the curve with a zero wave vector along the vortex [26]. As the chemical potential increases, the Fermi surface enlarges, and $\Phi_b(\mu)$ varies from 0 to 2π, defining a critical chemical potential such that $\Phi_b(\mu_C) = \pi$. Our results for the energies of the CdGM modes, which are
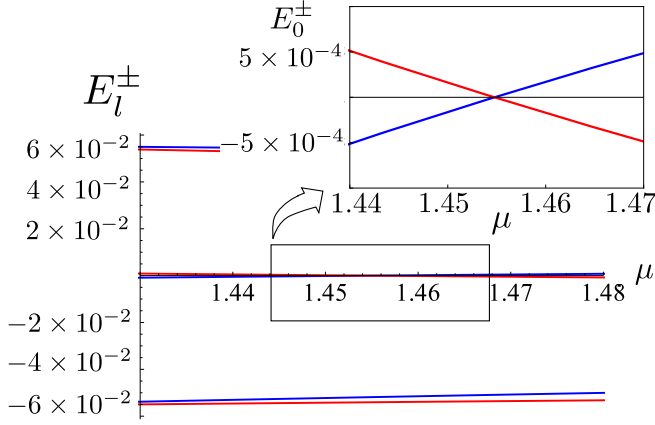
FIG. 1. (Color online) CdGM vortex-mode spectrum of the model from Ref. [26]. The parameters used in the calculation are described in Fig. 4 in Appendix A. We show the energies $E_l^+(\mu)$ (blue) and $E_l^-(\mu)$ (red) for $l = 0, \pm 1$ at chemical potentials close to $\mu_c \approx 1.455$. The inset displays the details for $l = 0$.

presented in Fig. 1, are consistent with the previous study of the phase transition in Refs. [26,28].

In terms of the CdGM eigenstates, Eq. (5) is written

$$\mathcal{S}_{\text{int}} = -\sum_{l,l',\sigma} \int d\tau \, \bar{\psi}_l^\sigma(\tau) \psi_{l'}^\sigma(\tau) \mathbf{R}(\tau) \cdot \mathbf{M}_{l,l'}^\sigma, \qquad (9)$$

where

$$\mathbf{M}_{l,l'}^\sigma = \int d^2 r \, \chi_l^\sigma(\mathbf{r})^\dagger \begin{pmatrix} 0 & \partial_\mathbf{r}\Delta \\ \partial_\mathbf{r}\Delta^\dagger & 0 \end{pmatrix} \chi_{l'}^\sigma(\mathbf{r}). \qquad (10)$$

Vortex fluctuations then generate the following self-energy for CdGM vortex modes which we calculate using the GW approximation [32] (details follow in Appendix B),

$$\Sigma_l^\sigma(i\tilde{\omega}) = \sum_{l',\alpha=\pm} \frac{A_{l;l'}^{\alpha;\sigma}}{\{i\tilde{\omega} - [\text{sgn}(\Xi_{l'}^{\alpha;\sigma})\omega_v] - \Xi_{l'}^{\alpha;\sigma}\}}. \qquad (11)$$

Here $A_{l;l'}^{\alpha;\sigma} \equiv \frac{|M_{l,l'}^{\alpha;\sigma}|^2}{m_v \omega_v}$ are reduced matrix elements with $M_{l,l'}^{\alpha;\sigma} = \frac{1}{2}(M_x + \alpha i M_y)_{l,l'}^\sigma$ and $\Xi_{l'}^{\alpha;\sigma} \equiv E_{l'}^\sigma + \alpha \omega_c/2$. For unit vorticity, angular momentum conservation implies that l is connected only to $l' = l + \alpha 1$ by such interactions. The energy scale introduced by $\omega_v \equiv \sqrt{\omega_0^2 + \omega_c^2/4}$ (and dominated by ω_0 as aforementioned), represents a "magnetoplasma" frequency in an Einstein model [17]. In Appendix B, we present closed formulas for these matrix elements.

One finally needs to evaluate the LDOS,

$$\rho(\mathbf{r},\omega) = \sum_{m,\sigma,l} |\langle \epsilon_m | \psi_{\sigma,l}^\dagger(\mathbf{r}) | N_0 \rangle|^2 \delta(\omega - \epsilon_m), \qquad (12)$$

where $|N_0\rangle$ is a N_0-particle ground state, $|\epsilon_m\rangle$ is a $(N_0 + 1)$-particle excited state (with generic quantum numbers m), and $\psi_{\sigma,l}^\dagger(\mathbf{r})$ is an electronic state creation operator at level l in sector σ. Using the vortex-mode eigenbasis, this can be written taking into account the effects of the vortex fluctuations in the

self-energy as

$$\rho(\mathbf{r},\omega) = \sum_{\sigma=\pm} \rho_\sigma(\mathbf{r},\omega), \qquad (13)$$

$$\rho_\sigma(\mathbf{r},\omega) = -\frac{1}{\pi} \text{Im} \sum_l \frac{|\mathbf{u}_l^\sigma(\mathbf{r})|^2}{\omega - E_l^\sigma - \Sigma_l^\sigma + i\epsilon}, \qquad (14)$$

$$= \sum_l |\mathbf{u}_l^\sigma(\mathbf{r})|^2 \delta[\omega - E_l^\sigma - \Sigma_l^\sigma(\omega)]. \qquad (15)$$

Through the perturbative interaction, the energy density profile of the CdGM modes is modified with part of the spectral weight from $\omega = E_l^\sigma$ being transferred to new "satellite" peaks in the LDOS [17]. Both the spectrum E_l^σ and the profile of $\mathbf{u}_l^\sigma(\mathbf{r})$ dramatically change the phenomenology described by (15) when the parent metallic state of the superconductor comes from doped TIs as compared with ordinary metals.

IV. TUNNELING CONDUCTANCE ANALYSIS

The local tunneling conductance is found at low temperatures by convolving the LDOS (15) with the derivative of the Fermi distribution function as

$$G(\mathbf{r},\omega) = -\frac{G_0}{\rho_0} \int d\omega' \rho(\mathbf{r},\omega + \omega') f'(\omega'). \qquad (16)$$

The normalization constant assumes an STM tip with constant DOS $\rho_0 = m_e/2\pi$ (for a free 2D electron gas) with the corresponding tunneling conductance G_0, and $f(\omega)$ is the Fermi-Dirac distribution. At very low temperatures, the tunneling conductance is equal to the LDOS, however still smoothed by the finite temperature effects.

Given the atomic level resolution of STM, we can safely focus at the density of states at the vortex core $\mathbf{r} = 0$. As seen in (6) and (7), the wave-function components may be expanded in terms of Bessel functions. In particular, at $\mathbf{r} = 0$, only Bessel functions of order zero have nonzero amplitude whereas all the other Bessel functions vanish. From our Fourier-Bessel expansion of the CdGM modes above, only $l = 0$ and, as a result of spin-orbit coupling, $l = 1$ modes have finite contributions in $\mathbf{u}_l^\sigma(\mathbf{r})$ at the origin.

The $l = 0$ states have energies $E_0^\sigma = \sigma \frac{\Delta^2}{E_F}(-\frac{1}{2} + \frac{\phi(\mu)}{2\pi})$. These energy levels may be pumped from negative to positive values (and vice versa) by changing the chemical potential, evolving the Berry phase from 0 to 2π. This novel feature leads to a change in sign in the factors of ω_v in the self-energy given in (11) when $l' = 0$, which determine the energies of the satellite peaks. As a result, the TPT manifests itself by a discontinuous change in the density of states by energies of order ω_v to energies of order $-\omega_v$.

Remarkably, the local spectrum at the vortex center breaks particle-hole symmetry. The origin of this lies in the spin-orbit coupling which, together with the BdG doubling, filtered only the states $l = 0, 1$ at this position, leaving out the $l = -1$ states. Naturally the full DOS is PH symmetric. These points will be considered again in Sec. V in the context of the effective theory for the vortex bound states after integration in the radial and angular directions.

Even more important, one notes that the Magnus force term associated with the vortex motion, whose amplitude

is proportional to ω_c, breaks the mirror symmetry which is connecting the PH sectors of the CdGM modes. As a result, the discontinuous transition of energy of the CdGM modes from the two σ sectors does not happen simultaneously at the same value of doping for both cases. This is essential for the change in the LDOS to be seen in this context as it provides an energy window over which the density of states at the energy of vortex oscillations is remarkably modified by the TPT. It is also important to note that, for other CdGM modes (such as the mode with $l = -1$ whose maximum amplitude is at $1/k_F \approx 10$ Å away from the center of the vortex), the opposite transition will happen. Given the spatial resolution of STM, however, the different modes should be resolvable.

To make the above claims regarding the peak jumping less abstract, let us concretely analyze the relevant contributions to the self-energy. As discussed, from angular momentum conservation $M_{l,l'}^{+;\sigma} = \delta_{l',l+1} M_{l,l+1}^{+;\sigma}$ and from $A_{l;l'}^{-;\sigma} = A_{l';l}^{+;\sigma}$ we can read the corresponding result for $\alpha = -$. These simplifications allow us to reduce the self-energy to just a couple of relevant pieces,

$$\Sigma_0^\sigma(\omega) = \frac{A_{0;1}^{+;\sigma}}{\left[\omega - \text{sgn}\left(\Xi_1^{+;\sigma}\right)\omega_v - E_1^\sigma - \omega_c/2\right]}$$
$$+ \frac{A_{-1;0}^{+;\sigma}}{\left[\omega - \text{sgn}\left(\Xi_{-1}^{-;\sigma}\right)\omega_v - E_{-1}^\sigma + \omega_c/2\right]}, \quad (17)$$

and

$$\Sigma_1^\sigma(\omega) = \frac{A_{1;2}^{+;\sigma}}{\left[\omega - \text{sgn}\left(\Xi_2^{+;\sigma}\right)\omega_v - E_2^\sigma - \omega_c/2\right]}$$
$$+ \frac{A_{0;1}^{+;\sigma}}{\left[\omega - \text{sgn}\left(\Xi_0^{-;\sigma}\right)\omega_v - E_0^\sigma + \omega_c/2\right]}. \quad (18)$$

To find the positions of the peaks, one solves

$$\omega - E_l^\sigma - \Sigma_l^\sigma(\omega) = 0. \quad (19)$$

The solutions are clearly sensitive to the sign of $\Xi_{l'}^{\alpha;\sigma} \equiv E_{l'}^\sigma + \alpha\omega_c/2$. As we do not have an estimate for the actual strength of the Magnus effect, to be definite, we take $\omega_c = \eta\frac{\Delta^2}{\mu}$. It is a simple job to notice that $\text{sgn}(\Xi_1^{+;\sigma}) = \text{sgn}(\Xi_2^{+;\sigma}) = +$ and $\text{sgn}(\Xi_{-1}^{-;\sigma}) = -$ for any value of the chemical potential. The sign of $\Xi_0^{-;\sigma}$, however, does depend on μ. This allows one to define a value $\bar{\mu}_\sigma$ at which $\text{sgn}(\Xi_0^{-;\sigma})$ changes. The structure of $\Sigma_1^\sigma(\omega)$ depends crucially on this. From the CdGM spectrum (8), we set $\Xi_0^{-;\sigma} = 0$ explicitly, finding

$$-\sigma + \left(\sigma\frac{\phi(\bar{\mu}_\sigma)}{\pi} - \eta\right) = 0$$
$$\Rightarrow \frac{\phi(\bar{\mu}_\sigma)}{\pi} = 1 + \eta\sigma, \quad (20)$$

where $\phi(\mu)$ is the Berry phase. As this phase grows monotonically from 0 to 2π, it is clear that the sector $\sigma = +$ has a sign change at values of μ larger than those of the $\sigma = -$ sector as long as $\eta \neq 0$. To summarize, this determines when each set of peaks will jump as function of μ. In Appendix C we explore this further also showing analytically that, at $\mathbf{r} = 0$, only the leftmost satellite peak from $l = 1$ will jump due to this sign change.
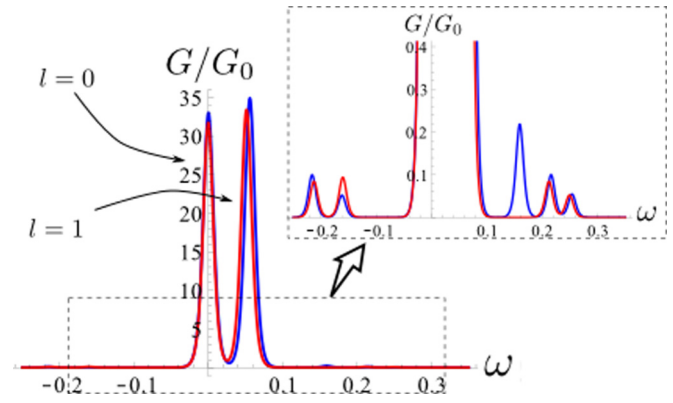

FIG. 2. (Color online) Tunneling conductance for $\mu < \bar{\mu}_\pm$ and $\mu > \bar{\mu}_\pm$ in blue and $\bar{\mu}_- < \mu < \bar{\mu}_+$ in red. The large central peaks correspond to $\omega \approx E_{l=0}^\pm$ and $\omega \approx E_{l=1}^\pm$ (the energies of the CdGM modes for the stationary vortex). The inset displays the effects of vortex fluctuations. The smaller satellite peaks appear at energies close to $\approx \pm\omega_v$. Red curves correspond to $\mu < \bar{\mu}_-$ or $\mu > \bar{\mu}_+$.

Figure 2 displays our main results. It shows the differential conductivity at the vortex center $G(\mathbf{r} = 0, \omega)$ (more details on the numerical parameters used here are given in Fig. 4 in Appendix A). Angular momentum conservation implies that each noninteracting energy level unfolds into a set of three peaks.

We present the differential conductance for three ranges of chemical potential $\mu < \bar{\mu}_\pm$ in blue, $\bar{\mu}_- < \mu < \bar{\mu}_+$ in red, and $\mu > \bar{\mu}_\pm$ in blue again, which appears to be identical to $\mu < \bar{\mu}_\pm$. This happens because the separation of the central peaks from $l = 1$ is $E_1^+ - E_1^+ = \delta[-1/2 + \phi(\mu)/2\pi]$, which cannot be resolved close to the phase transition (just as the peaks from $l = 0$ cannot be resolved at this situation.) In this situation, having a finite ω_c is crucial to observe all peaks and the discontinuous effects of the topological phase transition. The pattern in the LDOS should be, for each l and sector σ, of a large central peak located at E_l^σ with the two partners offset approximately by $\pm\Omega_l^\sigma$ with $\Omega_l^\sigma = \sqrt{(\omega_v + \delta + \omega_c/2)^2 + 2A_l^{+;\sigma}}$. In our case, a total of 12 peaks is expected for each value of the chemical potential (3 from $l = 0$, another 3 from $l = 1$, and twice this due to the two sectors), not all of them being resolvable due to thermal effects. The large peaks closest to $\omega = 0$ correspond to $\omega \approx E_{l=0,1}^\sigma$. The strength of the respective satellite peaks is suppressed by a ξ^{-5} factor, where ξ is the coherence length [17]. An inset displays the position of these peaks.

A remarkable behavior develops in the $l = 1$ satellite peaks (the rightmost small peaks at negative and positive frequencies). This is evidenced by the solitary blue peak at positive ω. It corresponds to the contribution coming from $\omega = E_1^- - \Omega_1^-$, whose position jumps from this value by approximately $2\omega_v$ as the chemical potential pumps the negative energy state at E_0^- into positive energies after crossing $\bar{\mu}_-$. Similarly, when μ moves above $\bar{\mu}_+$, the peak from $\omega = E_1^+ + \Omega_1^+$ jumps by $-2\omega_v$. In Appendix C we demonstrate that the approximate positions of the $l = 1$ peaks can be determined analytically.

Concerning the magnitude of the Magnus effect, if $\eta < 1$, the effects from the Magnus force are subdominant to the

CdGM energy gap, and the sensibility to which one needs to tune the (zero-temperature) chemical potential may again be beyond technical realization at the current time. If $\eta > 1$, on the other hand, as the evolution of the Berry phase is from 0 to 2π, the critical chemical potentials $\bar{\mu}_\sigma$ may not be captured as one tunes μ, and one will be bound to the regime of $\bar{\mu}_- < \mu < \bar{\mu}_+$, which is similar to the standard s-wave case (except for the multiplicities of peaks and apparent breaking of the PH constraint). As this seems to critically constrain the actual visualization of these effects in practice, we proceed now to consider some different situations in which one may actually control the energy difference between the $l = 1$ states for different $\sigma = \pm$ sectors. In this case, we will see that if this energy difference can be made larger, even at $\eta = 0$ one may be able to capture the closing and reopening of the energy gap from $l = 0$.

V. ONE-DIMENSIONAL WIRE MAPPING

To conclude our considerations, we would like to speculate about the realization of similar signatures of TPTs by quantum motion in other systems. Here we demonstrate concretely the claim from Ref. [26] stating that the vortex in superconducting doped TIs presents a topological phase transition equivalent to a Kitaev wire. We then proceed to show that, more generally, the Hamiltonian projected at the vortex states corresponds to a set of wires (or a single multiband wire) inheriting a first-neighbor mutual coupling from the vortex fluctuations in 3D. We then identify the important ingredients necessary to realize the discussed phenomena in the context of 1D topological systems.

A. Vortex Hamiltonian projection

Start with Hamiltonian (A1) from Appendix A keeping the z-direction terms. We also keep the vortex fluctuations to first order in the gradient of the superconducting pairing. We have

$$H_{\text{BdG}} = H^0_{\text{BdG}} + \Gamma_z P_z - \Gamma_0 \epsilon P_z^2 - \mathbf{R}(\tau) \cdot [\mathbf{\Lambda} \cdot \partial_\mathbf{r} \mathbf{\Delta}(\mathbf{r})], \quad (21)$$

$$\equiv H^0_{\text{BdG}} + H_z + V(\mathbf{r}). \quad (22)$$

We are going to project this into the lowest-energy sectors $\chi^\pm_{ln}(\mathbf{r})$ from (6) and (7). At finite z, we have $\chi^\pm_{ln}(\mathbf{r}) \rightarrow \chi^\pm_{ln_{\text{CdG}}}(\mathbf{r}) f^\pm_l(z)$, choosing the CdGM states with $n = n_{\text{CdG}}$. We will project the radial part of the Hamiltonian to find out what Hamiltonian gives the equations of motion for $f^\pm_l$. Considering the $\pm$ sectors then we have

$$\tilde{H}_{ll'} = \text{Proj}[H_{\text{BdG}}]_{ll'} \quad (23)$$

$$= \begin{pmatrix} E^+_l & 0 \\ 0 & E^-_l \end{pmatrix} \delta_{ll'} \quad (24)$$

$$+ \begin{pmatrix} H^{++}_{zll'} & H^{+-}_{zll'} \\ H^{-+}_{zll'} & H^{--}_{zll'} \end{pmatrix} \quad (25)$$

$$+ \begin{pmatrix} V^{++}_{ll'} & 0 \\ 0 & V^{--}_{ll'} \end{pmatrix}. \quad (26)$$

Notice that as $\langle \chi^+_l | \rho_x | \chi^-_l \rangle = \langle \chi^+_l | \rho_y | \chi^-_l \rangle = 0$, the fluctuating vortex potential becomes diagonal with respect to the $\pm$ sectors. This result is the same as we had found in our considerations at vanishing k_z, and we already know what this

term looks like,

$$\begin{pmatrix} V^{++}_{ll'} & 0 \\ 0 & V^{--}_{ll'} \end{pmatrix} = \mathbf{R}(\tau) \cdot \mathbf{M}^\sigma_{l,l'}, \quad (27)$$

with

$$\mathbf{M}^+_{l,l'} = d^2 r [\mathbf{u}^+_l(\mathbf{r})^\dagger \partial_\mathbf{r} \Delta \mathbf{v}^+_{l'}(\mathbf{r}) + \mathbf{v}^+_l(\mathbf{r})^\dagger \partial_\mathbf{r} \Delta^\dagger \mathbf{u}^+_{l'}(\mathbf{r})], \quad (28)$$

$$\mathbf{M}^-_{l,l'} = \int d^2 r [\mathbf{v}^+_l(\mathbf{r})^\dagger \partial_\mathbf{r} \Delta \mathbf{u}^+_{l'}(\mathbf{r}) + \mathbf{u}^+_l(\mathbf{r})^\dagger \partial_\mathbf{r} \Delta^\dagger \mathbf{v}^+_{l'}(\mathbf{r})]. \quad (29)$$

Due to the vortex structure in Δ, we are only coupling l to $l' = l \pm 1$.

Now we project H_z. To keep the notation short, we introduce 4×4 Dirac matrices $\boldsymbol{\alpha} = \tau_x \boldsymbol{\sigma}$ and $\beta = \tau_z \sigma_0$ as in Appendix A. It is easy to see that terms linear in P_z contribute off diagonally in the $\pm$ sectors whereas terms quadratic with P_z^2 contribute only diagonally. For these diagonal terms, we develop couplings,

$$\epsilon \rightarrow \begin{cases} \epsilon^+_l = \epsilon \int d^2 r [\mathbf{u}^+_l(\mathbf{r})]^* \beta \mathbf{u}^+_l(\mathbf{r}) - [\mathbf{v}^+_l(\mathbf{r})]^* \beta \mathbf{v}^+_l(\mathbf{r}), \\ \epsilon^-_l = \epsilon \int d^2 r [\mathbf{u}^-_l(\mathbf{r})]^* \beta \mathbf{u}^-_l(\mathbf{r}) - [\mathbf{v}^-_l(\mathbf{r})]^* \beta \mathbf{v}^-_l(\mathbf{r}). \end{cases} \quad (30)$$

Importantly, the sign of these couplings is the same, and the angular integration enforces $l = l_;$. For the off-diagonal terms we develop the couplings,

$$\tilde{\Delta}_l = \int d^2 r [\mathbf{u}^+_l(\mathbf{r})]^* \alpha^z \mathbf{u}^-_l(\mathbf{r}) - [\mathbf{v}^+_l(\mathbf{r})]^* \alpha^z \mathbf{v}^-_l(\mathbf{r}). \quad (31)$$

B. One-dimensional wire network

Adding up the matrix elements above gives the projected Hamiltonian,

$$\tilde{H}_{ll'} = \begin{pmatrix} E^+_l - \epsilon^+_l \partial^2_z & -i\, \tilde{\Delta}_l \partial_z \\ -i\, \tilde{\Delta}_l \partial_z & E^-_l + \epsilon^-_l \partial^2_z \end{pmatrix} \delta_{ll'} \quad (32)$$

$$+ \begin{pmatrix} \mathbf{R}(\tau) \cdot \mathbf{M}^+_{l,l'} & 0 \\ 0 & \mathbf{R}(\tau) \cdot \mathbf{M}^-_{l,l'} \end{pmatrix}. \quad (33)$$

For Hermiticity $\mathbf{M}^{\pm *}_{l,l'} = \mathbf{M}^\pm_{l',l}$. For the diagonal terms we may still use $E^-_{-l} = -E^+_l$ to write

$$\begin{pmatrix} E^+_l - \epsilon^+_l \partial^2_z & -i\, \tilde{\Delta}_l \partial_z \\ -i\, \tilde{\Delta}_l \partial_z & E^-_l + \epsilon^-_l \partial^2_z \end{pmatrix} \quad (34)$$

$$= \begin{pmatrix} E^+_l - \epsilon^+_l \partial^2_z & -i\, \tilde{\Delta}_l \partial_z \\ -i\, \tilde{\Delta}_l \partial_z & -(E^+_{-l} - \epsilon^-_l \partial^2_z) \end{pmatrix}. \quad (35)$$

As the signs of $\epsilon^\pm_l$ are the same, one can easily see that the $l = 0$ Hamiltonian is essentially the same as a Kitaev chain. For $l \neq 0$, on the other hand, the Hamiltonian does not describe a Kitaev chain. The PH symmetry is only present when $\pm l$, besides the $\sigma = \pm$ sectors, are taken into account. In this 1D projection, the contributions of the states in the whole radial direction are taken into account; in contrast, when probing the 3D system's LDOS at the center of the vortex, we filtered the contributions of $l = 0$ and $l = 1$ only. Because of this, PH symmetry is apparently broken in Fig. 2. These considerations

are more clearly seen by writing

$$
\begin{pmatrix}
E_l^+ - \epsilon_l^+ \partial_z^2 & -i\,\tilde{\Delta}_l \partial_z \\
-i\,\tilde{\Delta}_l \partial_z & E_l^- + \epsilon_l^- \partial_z^2
\end{pmatrix}
\tag{36}
$$

$$
\approx
\begin{pmatrix}
E_l^+ - \epsilon_l \partial_z^2 & -i\,\tilde{\Delta}_l \partial_z \\
-i\,\tilde{\Delta}_l \partial_z & -\left(E_{-l}^+ - \epsilon_l \partial_z^2\right)
\end{pmatrix}
$$

$$
\times
\begin{pmatrix}
E_l^+ - \epsilon_l \partial_z^2 & -i\,\tilde{\Delta}_l \partial_z \\
-i\,\tilde{\Delta}_l \partial_z & -\left(E_{-l}^+ - \epsilon_l \partial_z^2\right)
\end{pmatrix}
\tag{37}
$$

$$
= \frac{E_l^+ - E_{-l}^+}{2}\rho_0 + \rho_z\left(\frac{E_l^+ + E_{-l}^+}{2} - \epsilon_l \partial_z^2\right)
$$

$$
+ \rho_x(-i\,\tilde{\Delta}_l \partial_z).
\tag{38}
$$

The ρ_0 term does not vanish here (unless $l = 0$) as usually happens. To see that indeed the system is PH symmetric, one has to take into account the full second quantized Hamiltonian with all $\pm l$ pairs.

Likewise as above, the fluctuations may be written

$$
\begin{pmatrix}
\mathbf{R}(\tau) \cdot \mathbf{M}_{l,l'}^+ & 0 \\
0 & \mathbf{R}(\tau) \cdot \mathbf{M}_{l,l'}^-
\end{pmatrix}
$$

$$
= \mathbf{R}(\tau) \cdot \left(\frac{\mathbf{M}_{l,l'}^+ + \mathbf{M}_{l,l'}^-}{2}\right)\rho_0 + \mathbf{R}(\tau) \cdot \left(\frac{\mathbf{M}_{l,l'}^+ - \mathbf{M}_{l,l'}^-}{2}\right)\rho_z.
\tag{39}
$$

They couple diagonally in the $\sigma = \pm$ indices and bring up an apparently PH breaking term.

This projected Hamiltonian is then equivalent to a p-wave wire network. This is a very unusual network as PH symmetry actually connects different wires whereas each wire has PH symmetry actually broken. Although unusual, however, similar ideas have been considered in the literature [33]. It is remarkable, in any case, that the 3D physics we started with ends up in such an exotic 1D scenario.

C. TPT signatures in 1D

From the above results, we may identify the minimal ingredients necessary to magnify the signatures of TPTs in 1D systems by a mechanism similar to that considered in the vortex case. This minimal set of ingredients is undemanding. We list them in the context of Kitaev chains as there seems to be a recent focus of interest in the literature concerning Kitaev wires networks (see Ref. [34], for example). We stress, however, that the same ingredients would suffice for other 1D topological systems, such as Su-Schrieffer-Heeger wires or Kitaev superconducting:

(1) A pair of gapped wires, one of which is tunable through a TPT.

(2) A diagonal fluctuating coupling between them.

With these, one may reconstruct the important features of Eqs. (38) and (39). This situation is illustrated in Fig. 3.

Notice that the broken (PH) symmetry found in the projection on the vortex modes in the 3D scenario is not fundamental and is not included in our minimal list. It implies but a shift in the peaks in the spectrum, such as as in the large peaks from $l = 1$ in Fig. 2 and hence is unimportant. Also, a
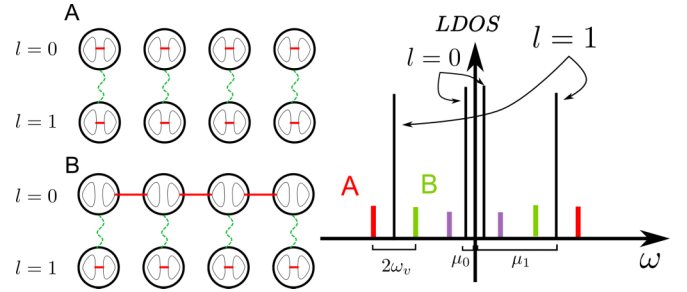

FIG. 3. (Color online) One-dimensional chain minimal model to study TPTs by quantum fluctuations. Large circles represent lattice complex fermions whereas the prolate circles represent the Majorana fermions inside. $l = 0$ represents a Kitaev chain which we drive through a topological phase transition whereas $l = 1$ is kept at a large gap. Situations A and B correspond to the two deep topological regimes. The chain site couplings are represented by green wriggly lines whereas Majorana hoppings are represented by the red lines. On the right, we display a schematic of the LDOS for this system. Large black peaks correspond to the peaks at the energy gaps $\pm\mu_l$ with $k = 0$, and dispersion effects are not considered. As there is a single fluctuating coupling between the chains, only a single satellite peak appears besides each $\pm\mu_l$. The purple peaks correspond to the satellite peaks of $\pm\mu_0$. The red and green peaks differ by $2\omega_v$, the fluctuation energy scale, and correspond to the two topological regimes A and B in the left figure. Even if the satellite peaks jump at the same time since the energy gap from wire $l = 1$ is large, one may resolve the distinct situations with the satellite peaks "outside" or inside the peaks from $\pm\mu_1$ as in the A or B situation, respectively. Notice that PH symmetry is explicitly respected in this context.

single pair of Kitaev chains is enough [the effects from $l = 2$ and $l = -1$ in (17) and (18) are not important]. This pair of wires could also be substituted by a single wire with a pair of low-energy bands. The tight-binding model for this is written

$$
H_{\text{Kit}}^l = -\mu_l \sum_j c_j^{l\dagger} c_j^l
$$

$$
- \frac{1}{2}\sum_j \left(t_l c_j^{l\dagger} c_{j+1}^l + \Delta_l e^{i\phi_l} c_j^l c_{j+1}^l + \text{H.c.}\right),
\tag{40}
$$

where μ_l is the chemical potentials, Δ_l is the SC pairings, ϕ_l is the corresponding SC phases, and t_l is the hopping amplitude for each wire. The index $l = 0,1$ labels the two chains. Upon BdG doubling, it is easy to demonstrate that this reduces to (38) in k space without the ρ_0 term.

As for the fluctuation part of the Hamiltonian, one may have simply

$$
U = \sum_j c_j^{0\dagger} \Phi(\tau) c_j^1 + \text{H.c.}
\tag{41}
$$

for a fluctuating coupling Φ. This should lead to similar self-energy corrections to the wires energies as (17) and (18), namely,

$$
\Sigma_{0,k}^\sigma(\omega) = \frac{A_{0;1}^\sigma}{\omega - \text{sgn}\left(E_{1,k}^{+;\sigma}\right)\omega_v - E_{1,k}^\sigma},
\tag{42}
$$

and

$$\Sigma_{1,k}^{\sigma}(\omega) = \frac{A_{1;0}^{\sigma}}{\omega - \text{sgn}(E_{0,k}^{-;\sigma})\omega_v - E_{0,k}^{\sigma}}, \qquad (43)$$

where σ gives the two Nambu components. The fluctuation frequency ω_v of Φ determines the new large energy scale. To find the positions of the peaks, one solves again

$$\omega - E_{l,k}^{\sigma} - \Sigma_{l,k}^{\sigma}(\omega) = 0, \qquad (44)$$

which now leads to a single satellite peak for each energy level.

Importantly, the effects of the Magnus force are not necessary in the 1D case, and hence, a single fluctuating parameter is enough. This happens because one may (by ramping the chemical potential transversally to the wires, for example) keep a single wire well away from the phase transition with a large gap. Suppose, for example, wire $l = 1$ is kept with a large gap. In this case, the satellite peaks from the two sectors in this wire will always stay far away from each other. This way, by tuning the chemical potential from wire $l = 0$, one can verify its phase transition by probing for the jumping in the satellite peaks of wire $l = 1$.

As a final comment, out of the p-wave superconductivity context, one might work similarly with a set of SSH wires. In this case, the Hamiltonian will be similar to as the BdG Hamiltonian considered so far with the caveat that the Nambu spinor now should be substituted by an ordinary spinor for a sublattice pseudospin degree of freedom. The gapping parameters in this case will be given by staggered hopping amplitudes and chemical potentials. Formally, the problem is the same, and one may extend the results discussed so far to this situation.

VI. CONCLUSIONS

Quantum fluctuations of vortex positions are ubiquitous and should manifest themselves at very low temperatures. We found out that, in the context of doped three-dimensional topological insulators, these fluctuations may be exploited to magnify the signatures of topological vortex quantum phase transitions. This manifests at the LDOS at the vortex core by energy peaks which discontinuously jump as function of the chemical potential. This finding also determined characteristic features of the low-energy Caroli–de Gennes–Matricon modes in this system which make them stand out as very distinct from standard s-wave Caroli–de Gennes modes, such as their spatial distribution and effects in the LDOS at the vortex core. Finally, our results also point to the possibility of capturing the effects of Magnus forces acting on the vortices, whose magnitude is directly related to the chemical potential values in which the topological phase transition induces peak position shifts.

The frequency of the position fluctuations plays an important role as it sets the scale for the peak jumps. In the context of high-temperature superconductors, there are reports of this energy scale going up to meV [35]. It is important to point out that this frequency can be controlled to some extent and indeed increased depending on the properties of the vortex pinning potential. Recent developments in doping TIs with niobium, which leads to the formation of magnetic moments in the bulk superconducting TI, can provide stronger pinning and so larger frequencies for the vortex fluctuation [36]. Measured physical

values of the vortex fluctuation frequencies and Magnus force frequency in this system are not known to us at this point.

Cryogenic STM measurements are fundamental to uncover the discussed signatures. Situations with lighter and smaller vortices, whose zero point motion effects would be stronger, could also be arranged as the vortex size is known to be strongly sensitive to temperature and magnetic-field strength [37]. For vortices of too minute sizes, however, the Taylor expansion method deployed here to derive the interactions is not precise. In such cases, different approaches to the problem, such as that used in Ref. [18], are necessary in order to obtain trustworthy predictions. Also, a proper account for the effects of dispersion along the vortex may need detailed attention. It is beyond the scope of this paper to consider these.

Finally, we studied the local physics along the vortex core. Projecting the Hamiltonian with the Caroli–de Gennes–Matricon wave functions we demonstrated explicitly that the vortex line behaves as a Kitaev chain with the corresponding topological phase transition. Further studying how the vortex position fluctuations are projected into this system allowed us to find some key ingredients which one may use to obtain new signatures of topological phase transitions in one dimension. A promising scenario lies in the study of the density of states upon fluctuations of the transversal coupling between a pair of neighboring gapped wires. Again, effects of dispersion along the wires still deserve attention.

ACKNOWLEDGMENTS

APPENDIX A: CAROLI–dE GENNES MODES

Here we present our numerical method to derive the spectrum of vortex modes for a stationary vortex in a doped superconducting topological insulator [26] and compare the solutions with an analytical approximated ansatz. The latter will be used to study the effect of vortex quantum zero point motion on the vortex spectrum.

The method which we apply is analogous to the one introduced by Refs. [17,31] in the context of ordinary superconductors. We start by considering a cylinder space, infinite in the z direction. The Bogoliubov–de Gennes Hamiltonian with a static vortex centered at the origin reads

$$H_{\text{BdG}}^0 = v_D \boldsymbol{\Gamma} \cdot \mathbf{P} - \mu \Sigma + \Gamma_0(m - \epsilon P^2) - \boldsymbol{\Lambda} \cdot \boldsymbol{\Delta}(\mathbf{r}), \quad (A1)$$

where the "Dirac velocity" v_D is set to 1 throughout our derivations and recovered to simplify the numerical calculations later. The Dirac matrices obey $\{\Gamma_\mu, \Gamma_\nu\} = 2\delta_{\mu\nu}$, $\{\Lambda_a, \Lambda_b\} = 2\delta_{ab}$, and $[\Gamma_\mu, \Sigma] = \{\Lambda_a, \Sigma\} = 0$. Notice Σ commutes with the kinetic Hamiltonian and is not a mass term. In our basis, a choice for the representation follows:

$$\boldsymbol{\Gamma} = \rho_z \tau_x \boldsymbol{\sigma}, \qquad \boldsymbol{\Lambda} = \boldsymbol{\rho} \tau_0 \sigma_0, \qquad (A2)$$

$$\Gamma_0 = \rho_z \tau_z \sigma_0, \qquad \Sigma = \rho_z \tau_0 \sigma_0, \qquad (A3)$$

with Nambu, orbital, and spin spaces described by ρ, τ, and σ Pauli matrices, respectively. Here $\mathbf{\Delta}(\mathbf{r}) = \Delta_0(r)(\cos\theta, \sin\theta)$ gives the pairing with a $\Delta_0(r) = \Delta_0 \tanh(r/\xi)$ profile to be concrete.

The vortex runs along the z direction, and translation invariance allows us to consider the k_z momentum; with the understanding that only $k_z = 0, \pi$ are topologically relevant, we take $k_z = 0$ since we are looking only for the low-energy Caroli–de Gennes–Matricon modes [26].

The Hamiltonian commutes with the generalized angular momentum operator $\tilde{L}_z = -i\partial_\theta - \frac{S_z + \Sigma}{2}$, where $\Gamma_x\Gamma_y = i\rho_0\tau_0\sigma_z \equiv iS_z$. This allows writing the solution spinors as

$$\chi_{l,n}(\mathbf{r}) = \frac{1}{\sqrt{2\pi}} \exp\left[-i\left(l - \frac{S_z + \Sigma}{2}\right)\theta\right]\phi_{l,n}(r), \quad \text{(A4)}$$

where l is an integer representing the standard angular momentum and n labels the many possible energies for a given l. At $k_z = 0$, the Hamiltonian obeys a further symmetry given by $\mathcal{M} = \rho_0\tau_z\sigma_z$. Noticing that $\{\mathcal{C}, \mathcal{M}\} = 0$ and naturally $\{\mathcal{C}, H_{\mathrm{BdG}}\} = 0$, we see that the eigenvalues of $\mathcal{M}$ also label particle and hole partners. This allows one to separate $\phi_{l,n}(r)$ in four-spinors $\phi_{l,n}^{\pm}(r)$, obeying corresponding Schrödinger's equations with projected Hamiltonians $H^{\pm}$ [26],

$$H^{\pm}\phi_{l,n}^{\pm} = E_{l,n}^{\pm}\phi_{l,n}^{\pm}. \quad \text{(A5)}$$

We focus on $\phi_{l,n}^{+}$ noticing that $\phi_{l,n}^{-} = \mathcal{C}\phi_{-l,n}^{+}$ with $E_{l,n}^{-} = -E_{-l,n}^{+}$. The 4×4 reduced radial Hamiltonian reads

$$H^{+} = \rho_z v_y\left[-i\partial_r + iv_z\frac{1}{r}\left(l - \frac{\rho_z + v_z}{2}\right)\right] - \mu\rho_z - \Delta_0(r)\rho_x$$
$$+ \rho_z v_z\left\{m + \epsilon\left[\frac{1}{r}\partial_r r\,\partial_r - \frac{1}{r^2}\left(l - \frac{\rho_z + v_z}{2}\right)^2\right]\right\}. \quad \text{(A6)}$$

Here v Pauli matrices represent a spin-orbital coupled space. Noticing that

$$a_l = \left(\partial_r + \frac{l}{r}\right), \quad \text{(A7)}$$

$$a_l^{\dagger} = -\left(\partial_r - \frac{l-1}{r}\right) \quad \text{(A8)}$$

act as operators which lower and raise the level of Bessel functions (and $a_l^{\dagger}a_l$ gives the Bessel differential operator itself), it is easy to find a proper basis to expand the states. If $\Delta_0 = 0$, we recover a pair of topological insulator Hamiltonians with spectra given by $E_k^{\pm\pm} = \pm\mu \pm \sqrt{k^2 + m_k^2}$ with $m_k = m - \epsilon k^2$ and k as a "radial linear momentum" quantum number. In the weak pairing approximation, since we are interested only in the lowest-energy modes, we solve for the eigenstates of the TI Hamiltonian using the ladder operators above and project out the bands from E_k^{++} and E_k^{--}. Thus Fourier-Bessel expand the radial wave functions as

$$\phi_{l,n}^{+} \approx \int dk \begin{pmatrix} c_{l,k}^n f_{l,k}(r) \\ d_{l,k}^n g_{l,k}(r) \end{pmatrix}, \quad \text{(A9)}$$

where

$$f_{l,k}(r) = \frac{1}{\sqrt{\mathcal{N}_{k,l}^{+}}}\begin{pmatrix} kJ_{l-1}(kr) \\ \left(m_k - \sqrt{m_k^2 + k^2}\right)J_l(kr) \end{pmatrix},$$

$$g_{l,k}(r) = \frac{1}{\sqrt{\mathcal{N}_{k,l}^{-}}}\begin{pmatrix} \left(m_k + \sqrt{m_k^2 + k^2}\right)J_l(kr) \\ -kJ_{l+1}(kr) \end{pmatrix}, \quad \text{(A10)}$$

and $\mathcal{N}_{k,l}^{\pm}$ are normalization constants given by $\mathcal{N}_k^{\pm} = 2(k^2 + m_k^2 \mp m_k\sqrt{m_k^2 + k^2})\int_0^{\infty} r\,dr\,J_l(kr)J_l(kr)$. The Schrödinger equation reduces to

$$\begin{pmatrix} T^{-} & \Delta \\ \Delta^T & T^{+} \end{pmatrix}\Phi_{ln}^{+} = E_{l,n}^{+}(\mu)\Phi_{ln}^{+}, \quad \text{(A11)}$$

where

$$T_{k,k'}^{\mp} = \left(\mp\mu \pm \sqrt{k^2 + m_k^2}\right)\delta(k - k'), \quad \text{(A12)}$$

with respective signs,

$$\Delta_{l,k,k'} = \int r\,dr\,f_{l,k}^T(r)\begin{pmatrix} \Delta_0(r) & 0 \\ 0 & \Delta_0(r) \end{pmatrix}g_{l,k'}(r), \quad \text{(A13)}$$

and the spinor is $\Phi_{ln}^{+} = (\{c_{lk}^n\}, \{d_{lk}^n\})^T$.

In terms of our original variables, the wave functions are then written

$$\chi_{ln}^{+}(\mathbf{r}) = \begin{pmatrix} \mathbf{u}_{ln}^{+}(\mathbf{r}) \\ \mathbf{v}_{ln}^{+}(\mathbf{r}) \end{pmatrix}, \quad \text{(A14)}$$

where

$$\mathbf{u}_{ln}^{+}(\mathbf{r}) = \int dk\,\frac{c_{lk}^n}{\sqrt{2\pi\mathcal{N}_k^{+}}}\begin{pmatrix} e^{-i(l-1)\theta}kJ_{l-1}(kr) \\ 0 \\ 0 \\ e^{-i(l-1)\theta}kJ_{l-1}(kr) \end{pmatrix}, \quad \text{(A15)}$$

$$\mathbf{v}_{ln}^{+}(\mathbf{r}) = \int dk\,\frac{d_{lk}^n}{\sqrt{2\pi\mathcal{N}_k^{-}}}\begin{pmatrix} e^{-il\theta}\left(m_k + \sqrt{m_k^2 + k^2}\right)J_l(kr) \\ 0 \\ 0 \\ ke^{-i(l+1)\theta}J_{l+1}(kr) \end{pmatrix}, \quad \text{(A16)}$$

and the mirror (particle-hole) partners are built from $\chi_{ln}^{-}(\mathbf{r}) = \mathcal{C}\chi_{-ln}^{+}(\mathbf{r})$.

We then fix a finite radius R for the cylinder size which forces us to discretized $k \to \alpha_{l,j}/R$ where $\alpha_{l,j}$ are the jth Bessel zeros at each l subspace. We fix a UV cutoff at some (large) N_0th Bessel zero. Diagonalizing the resulting Hamiltonian leads to the spectrum shown in Fig. 4. One sees two in-gap modes, one corresponding to outer edge modes, which we neglect, whereas the other corresponds to our desired vortex modes as can be checked by plotting their respective probability densities.

For the low-energy states, $n \equiv n_{\mathrm{CdG}}$ (a label which we drop from now on), one may check that the spectrum follows the
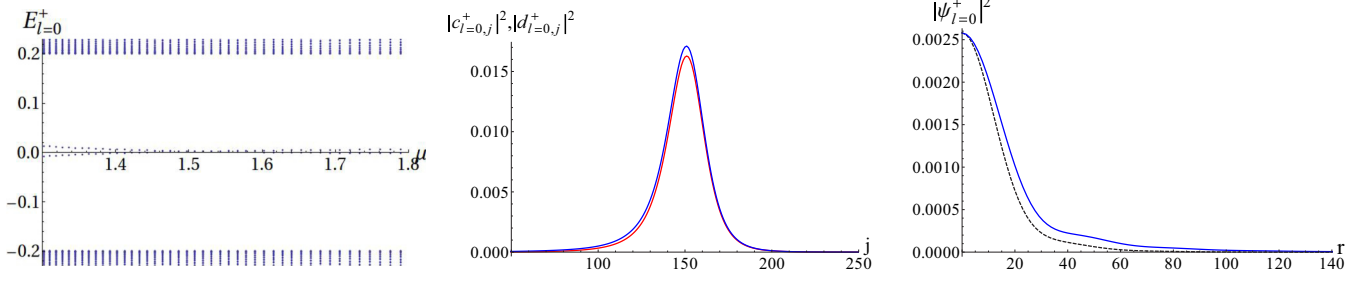
FIG. 4. (Color online) Numerical results for the lowest CdGM mode $l = 0$ in the $\sigma = +$ sector. Fixing the parameters demands some care as one needs to consider a large enough region of k space as to capture the TI band inversion while considering Fermi energies large to guarantee $k_F \xi > 1$ and at the same time close to the critical value of $\mu_C \sim v_D \sqrt{m/\epsilon}$. For all figures we use (disk size) $R = 5000$, (number of modes) $N_0 = 300$, $m = 1$, $\epsilon = 120$, and $\Delta_0 = 0.2$ and use units with Dirac velocity $v_D = 15$. Thus $\xi = v_D/\pi \Delta_0 \sim 23$, and the expected critical potential falls at $\mu_C \sim 1.37$. (Left) Energy spectrum as a function of the chemical potential. A clear gap is seen at 0.2 with in-gap modes. The two modes correspond to a vortex bound mode with a positive slope and a gapless expected edge mode as can be checked plotting the probability density in real space. (Middle) Momentum space distribution of the positive slope in-gap mode at a chemical potential close to the critical. The red and blue curves are associated with $|c_{l=0,j}|^2$ and $|d_{l=0,j}|^2$ at discrete momenta $j \leftrightarrow k_j = \alpha_{l,j}/R$, respectively. (Right) Probability density in the radial direction. The blue solid curve corresponds to (A14) whereas the dashed line corresponds to (A18), demonstrating that our ansatz is indeed a good approximation for the CdGM mode wave functions.

expected

$$E_l^{\pm} = \frac{\Delta^2}{E_F} \left(l \mp \frac{1}{2} \pm \frac{\phi(\mu)}{2\pi} \right), \quad \text{(A17)}$$

where $\phi(\mu)$ is the chemical-potential-dependent Berry's phase. At the critical chemical potential $\phi(\mu_C) = \pi$. It grows monotonically from 0 to 2π with the chemical potential. Noticing that the values of the momentum in k space are strongly localized at its Fermi value k_F as one might expect, it is easy to guess an analytical approximation for the wave functions which satisfies their desired asymptotic behaviors (see Ref. [26] for details). We have

$$\chi^+ = \mathcal{C} \exp\left[-\frac{2}{v_F} \int_0^r dr' \Delta(r') \right] \begin{pmatrix} f(\theta, r) \\ g(\theta, r) \end{pmatrix}, \quad \text{(A18)}$$

where

$$f(\theta, r) = \frac{\mathcal{C}}{\sqrt{2\pi N_{k_F}^+}} \begin{pmatrix} e^{-i(l-1)\theta} k_F J_{l-1}(k_F r) \\ 0 \\ 0 \\ e^{-il\theta}\left(m_{k_F} - \sqrt{m_{k_F}^2 + k_F^2}\right) J_l(k_F r) \end{pmatrix},$$

(A19)

$$g(\theta, r) = \frac{\mathcal{C}}{\sqrt{2\pi N_{k_F}^-}} \begin{pmatrix} e^{-il\theta}\left(m_{k_F} + \sqrt{m_{k_F}^2 + k_F^2}\right) J_l(k_F r) \\ 0 \\ 0 \\ e^{-i(l+1)\theta} k_F J_{l+1}(k_F r) \end{pmatrix},$$

(A20)

and the new normalizations read

$$N_{k_F}^{\pm} = 2\left(k_F^2 + m_{k_F}^2 \mp m_{k_F}\sqrt{m_{k_F}^2 + k_F^2}\right). \quad \text{(A21)}$$

Here, $\mathcal{C}$ is a normalization constant of order $(k_F/\xi)^{1/2}$. In the main text we compare the analytical and numerical results for the wave functions at $l = 0$ and $\mu \approx \mu_c$ showing that the approximation indeed works.

APPENDIX B: ELECTRONIC EFFECTIVE INTERACTION AND SELF-ENERGY

In this section we compute explicitly the electronic self-interaction due to the interplay with the vortex fluctuations and the corresponding self-energy in the GW approximation.

We start from the vortex effective action of the main text in frequency space,

$$\mathcal{S}_{\text{eff}}^{\text{vortex}} = \frac{m_v}{2} \int \frac{d\omega}{2\pi} \mathbf{R}^{\dagger}(i\omega) \begin{pmatrix} \omega^2 + \omega_0 & \omega_c \omega \\ -\omega_c \omega & \omega^2 + \omega_0^2 \end{pmatrix} \mathbf{R}(i\omega),$$

(B1)

and work at zero temperature. Noticing that $\mathbf{R}^{\dagger}(i\omega) = \mathbf{R}(-i\omega)$, we introduce a basis $R_{\pm}(i\omega) = \frac{R_x(i\omega) \pm i R_y(i\omega)}{\sqrt{2}}$, which diagonalizes the Lagrangian density as

$$\mathcal{S}_{\text{eff}}^{\text{vortex}} = \int \frac{d\omega}{2\pi} [R_-^{\dagger}(i\omega), R_+^{\dagger}(i\omega)] \mathbb{D}_0^v(i\omega)^{-1} \begin{pmatrix} R_-(i\omega) \\ R_+(i\omega) \end{pmatrix},$$

(B2)

with

$$\mathbb{D}_0^v(i\omega) = \begin{pmatrix} D_-^{-1} & 0 \\ 0 & D_+^{-1} \end{pmatrix}, \quad \text{(B3)}$$

and the Green's functions $D_{\mp}(i\omega) = \frac{m_v}{2}[(\omega \pm i\omega_c/2)^2 + \omega_v^2]$. This sets the two important energy scales dictated by the vortex fluctuations as ω_c from the Magnus force, and $\omega_v = \sqrt{\omega_0^2 + \omega_c^2/4}$ from the harmonic trap.

As discussed in the former section, the low-energy modes divide into two Hilbert space sectors related by a z-mirror/particle-hole symmetry. Each sector is subject to an effective potential arising after the integration of the vortex

zero-dimensional field theory. From Eqs. (4) we may write

$$e^{-V_{\rm eff}^\sigma[\bar\psi_l^\sigma,\psi_l^\sigma]} \propto \int \mathcal{D}[\mathbf{R}] \exp\left[-S_{\rm eff}^{\rm vortex} + \int d\tau \sum_{l,l'} \mathbf{R}(\tau) \cdot \mathbf{M}_{l,l'}^\sigma \bar\psi_l^\sigma(\tau)\psi_{l'}^\sigma(\tau) \right]. \tag{B4}$$

Define $\mathbf{U}^\sigma(i\omega) = \sum_{l,l'} \int \frac{d\nu}{2\pi} \mathbf{M}_{l,l'}^\sigma \bar\psi_l^\sigma(i\nu+i\omega)\psi_{l'}^\sigma(i\nu)$ and rewrite the scalar products in terms of the $R_\pm(i\omega)$ coordinates and $M^{\alpha;\sigma} = \frac{1}{2}(M_x + \alpha i M_y)$ with $\alpha = \pm$. Then

$$M_{l,l'}^{+;\sigma} = \left(M_{l',l}^{-;\sigma}\right)^* = \int d^2r \left[\mathbf{u}_l^\sigma(\mathbf{r})^\dagger \partial_{\bar z} \Delta \mathbf{v}_{l'}^\sigma(\mathbf{r}) + \mathbf{v}_l^\sigma(\mathbf{r})^\dagger \partial_{\bar z} \Delta^\dagger \mathbf{u}_{l'}^\sigma(\mathbf{r}) \right]. \tag{B5}$$

This allows, with a careful consideration of positive and negative frequencies, integration over the vortex degrees of freedom, leading to the effective action of the electronic modes as

$$S_{\rm eff}^\sigma[\bar\psi^\sigma,\psi^\sigma] = \sum_l \int \frac{d\tilde\omega}{2\pi} \bar\psi_l^\sigma(i\tilde\omega)\left(i\tilde\omega - E_l^\sigma\right)\psi_l^\sigma(i\tilde\omega) - \int \frac{d\tilde\omega}{2\pi}\left[\frac{1}{4}(U_-^{\sigma\dagger} D_+^{-1} U_-^\sigma + U_+^{\sigma\dagger} D_-^{-1} U_+^\sigma) \right], \tag{B6}$$

where $U_\alpha^\sigma = \frac{1}{2}(U_x^\sigma + \alpha i U_y^\sigma)$. A tedious but straightforward simplification leads to the effective electronic self-interaction,

$$V_{\rm eff}^\sigma\left[\bar\psi_l^\sigma,\psi_l^\sigma\right] = \frac{1}{2}\sum_{l,l',n,n'} \int \frac{d\tilde\omega}{2\pi} \int \frac{d\tilde\nu}{2\pi} \int \frac{d\tilde\nu'}{2\pi} \bar\psi_l^\sigma(i\tilde\nu + i\tilde\omega)\bar\psi_n^\sigma(i\tilde\nu' - i\tilde\omega)V_{l,l',n,n'}^\sigma(i\tilde\omega)\psi_{l'}^\sigma(i\tilde\nu)\psi_{n'}^\sigma(i\tilde\nu'), \tag{B7}$$

where

$$V_{l,l',n,n'}^\sigma(i\tilde\omega) = -\frac{1}{m_v} \sum_{\alpha=\pm} \left[\frac{\left(M_{l,l'}^{\alpha;\sigma}\right)^\dagger M_{n,n'}^{\alpha;\sigma}}{\left[(\tilde\omega + \alpha i\omega_c/2)^2 + \omega_v^2\right]} \right]. \tag{B8}$$

From (A14), the matrix elements have a simple form

$$M_{l,l'}^{\alpha;\sigma} = \int d^2r \left[\mathbf{u}_m^\sigma(\mathbf{r})^\dagger \partial_{\bar z} \Delta \mathbf{v}_{m'}^\sigma(\mathbf{r}) + \mathbf{v}_m^\sigma(\mathbf{r})^\dagger \partial_{\bar z} \Delta^\dagger \mathbf{u}_{m'}^\sigma(\mathbf{r}) \right], \tag{B9}$$

which also shows the convenient fact that $M_{l,l'}^{+;\sigma} = M_{l',l}^{-;\sigma*}$.

Interaction (B8) shows a screened Coulomb-like retarded interaction. The self-energy in the GW approximation comes now from a simple one-loop calculation,

$$\Sigma_l^\sigma(i\tilde\omega) = -\sum_{l'} V_{l,l,l',l'}^\sigma(0) \int_\omega G_l^{0\sigma}(i\omega)$$

$$+ \sum_{l'} \int_\omega V_{l,l',l',l}^\sigma(i\tilde\omega - i\omega)G_{l'}^{0\sigma}(i\omega). \tag{B10}$$

The first term vanishes. The second must be considered with care as the pole structure is sensitive to the structure of the

energy levels. An integration over the complex plane gives the self-energy of the main text,

$$\Sigma_l^\sigma(i\tilde\omega) = \sum_{l'}\sum_{\alpha=\pm} \frac{A_{l;l'}^{\alpha;\sigma}}{\left\{ i\tilde\omega - \left[\operatorname{sgn}(\Xi_{l'}^{\alpha;\sigma})\omega_v + E_{l'}^\sigma \right] - \alpha\omega_c/2 \right\}}, \tag{B11}$$

where $A_{l;l'}^{\alpha;\sigma} \equiv \frac{|M_{l,l'}^{\alpha;\sigma}|^2}{m_v\omega_v}$ and $\Xi_{l'}^{\alpha;\sigma} \equiv E_{l'}^\sigma + \alpha\omega_c/2$.

To calculate the matrix elements one may make use of the Feynman-Hellman relations, adapted to our Hamiltonian and in a finite cylinder. A long calculation making full use of Bessel function relations finally gives

$$M_{l,l'}^{+;+} = \frac{\delta_{l',l+1}}{2} \sum_{j,j'} c_{lj}\left[(E_{l+1}^+ - E_l^+)\mathcal{K}_{j,j'}^{l+} - \mathcal{L}_{j,j'}^{l+}\right]c_{l+1j'}$$

$$+ \frac{1}{2}\sum_{j,j'} d_{lj}\left[(E_{l+1}^+ - E_l^+)\mathcal{K}_{j,j'}^{l-} - \mathcal{L}_{j,j'}^{l-}\right]d_{l+1j'}, \tag{B12}$$

with

$$\mathcal{K}_{j,j'}^{l\pm} = \operatorname{sgn}(l+1/2)(-1)^{j-j'} \frac{\alpha_{jl}\alpha_{j'l+1}}{R(\alpha_{j'l+1}^2 - \alpha_{jl}^2)} \frac{\mathcal{M}_{jl}^\pm \mathcal{M}_{j'l+1}^\pm + \left(\frac{\alpha_{j'l+1}}{R}\right)^2}{\sqrt{\left[\left(\frac{\alpha_{jl}}{R}\right)^2 + \mathcal{M}_{jl}^\pm\right]\left[\left(\frac{\alpha_{j'l+1}}{R}\right)^2 + \mathcal{M}_{j'l+1}^\pm\right]}}, \tag{B13}$$

and

$$\mathcal{L}_{j,j'}^{l\pm} = \operatorname{sgn}(l+1/2)(-1)^{j-j'} \frac{2\epsilon\alpha_{jl}\alpha_{j'l+1}}{R^3} \frac{\left(\frac{(l\mp1)(l+1\mp1)}{R^2} + \mathcal{M}_{jl}^\pm \mathcal{M}_{j'l'}^\pm\right)}{\sqrt{\left[\left(\frac{\alpha_{jl}}{R}\right)^2 + \mathcal{M}_{jl}^\pm\right]\left[\left(\frac{\alpha_{j'l+1}}{R}\right)^2 + \mathcal{M}_{j'l+1}^\pm\right]}}. \tag{B14}$$

Here, R is the cylinder finite radius, α_{jl} is the jth zero of the lth Bessel function, and $\mathcal{M}_{jl}^\pm = m_{j,l}^2 \mp m_{j,l}\sqrt{m_{j,l}^2 + \left(\frac{\alpha_{jl}}{R}\right)^2}$ with $m_{j,l} = m - \epsilon\alpha_{jl}/R$. The other matrix elements may be found from

$$M_{l,l'}^{\alpha;-} = -M_{-l',-l}^{\alpha;+}, \tag{B15}$$

$$M_{l,l'}^{-;\sigma} = \left(M_{l',l}^{+;\sigma}\right)^* \equiv \left(M_{l,l'}^{+;\sigma}\right)^\dagger. \tag{B16}$$

These expressions are very similar to Bartosch's, corrected for spin-orbit coupled states.

APPENDIX C: PEAK ANALYSIS

Here we describe in detail the determination of the relative sizes and positions of the tunneling conductance peaks. We start rewriting

$$\rho(\mathbf{r},\omega) = \sum_{\sigma=\pm} \rho_\sigma(\mathbf{r},\omega), \tag{C1}$$

$$\rho_\sigma(\mathbf{r},\omega) = -\frac{1}{\pi} \text{Im} \sum_l \frac{\left|\mathbf{u}_l^\sigma(\mathbf{r})\right|^2}{\omega - E_l^\sigma - \Sigma_l^\sigma + i\epsilon}, \tag{C2}$$

using the vortex-mode eigenbasis. STM measurements probe the tunneling conductance,

$$G(\mathbf{r},\omega) = -\frac{G_0}{\rho_0} \int d\omega' \rho(\mathbf{r},\omega+\omega') f'(\omega'), \tag{C3}$$

where $f(\omega)$ is the Fermi distribution.

At zero temperature this reduces simply to the LDOS, up to a constant. At finite temperature we may write

$$G(\mathbf{r},\omega)/G_0 = -\frac{1}{\rho_0} \sum_{l,\sigma=\pm} \sum_i \frac{\left|u_l^\sigma(\mathbf{r})\right|^2}{\left|1 - \frac{\partial \Sigma_l^\sigma(\omega_{l,\sigma,0}^i)}{\partial \omega}\right|} \tag{C4}$$

$$\times f'\left(\omega_{l,\sigma,0}^i - \omega\right), \tag{C5}$$

where $\omega_{l,\sigma,0}^i$ is the ith solution to

$$\omega - E_l^\sigma - \Sigma_l^\sigma(\omega) = 0. \tag{C6}$$

This represents a cubic equation, thus with three solutions. Whereas (C6) determines where are the relative positions of the peaks in energy space, the derivatives $\frac{\partial \Sigma_l^\sigma(\omega_{l,\sigma,0}^i)}{\partial \omega}$ will fix the peaks relative sizes.

We focus most of our analysis on $|\mathbf{r}| = 0$, which, from (A14), means that only the states with $l = 0, 1$ give nonvanishing contributions. The relevant self-energy contributions were considered in the main text in Eqs. (17) and (18). To determine the relative sizes and positions of the peaks, we examine the derivatives of the self-energy as well as Eq. (C6) explicitly.

1. Peak sizes

The derivatives of the self-energies read, after some simplification,

$$\frac{d\Sigma_1^\sigma(\omega)}{d\omega} = -\frac{A_{1;2}^{+;\sigma}}{\left(\Delta\omega_1^\sigma - \delta - \omega_c/2 - \omega_v\right)^2}$$

$$-\frac{A_{0;1}^{+;\sigma}}{\left[\Delta\omega_1^\sigma + \delta + \omega_c/2 - \sigma \,\text{sgn}(\mu - \bar{\mu}_\sigma)\omega_v\right]^2}, \tag{C7}$$

$$\frac{d\Sigma_0^\sigma(\omega)}{d\omega} = -\frac{A_{0;1}^{+;\sigma}}{\left(\Delta\omega_0^\sigma - \delta - \omega_c/2 - \omega_v\right)^2}$$

$$-\frac{A_{-1;0}^{+;\sigma}}{\left(\Delta\omega_0^\sigma + \delta + \omega_c/2 + \omega_v\right)^2}, \tag{C8}$$

where $\Delta\omega_l^\sigma = \omega - E_l^\sigma$ and δ is the minigap.

The matrix elements are much smaller than the other physical quantities. Dimensional analysis and explicit manipulation

of (B5) shows that, at constant ω_v/Δ_0, these overlaps sizes depend on the coherence length as ξ^{-5} [17]. The peak sizes, nevertheless, are going to be sensitive to $A_{l;l'}^{\alpha;\sigma}$. As will be seen in the next subsection, the satellite peak positions are dominated by the vortex oscillation frequency ω_v. Plugging in $\Delta\omega_l^\sigma \approx 0$ or $\Delta\omega_l^\sigma \approx \pm\omega_v$ one sees that $d\Sigma_l^\sigma(\omega)/d\omega$ is small (concretely it is $\propto A_{l,l'}^{+;\sigma}/\omega_v^2 \ll 1$) at $\Delta\omega_0^+ \approx 0$ although it may be larger at $\Delta\omega_0^\sigma \approx \pm\omega_v$, going as $\sim -A_{0;1}^{+;+}[\frac{1}{s^2}]$, where $s = \frac{\delta+\omega_c/2}{2\omega_v}$. The latter case reduces the size of the satellite peaks greatly from $l = 0$, similarly as pointed by Bartosch and Sachdev [17].

2. Peak positions

Our last goal is to explain the positions of the peaks as functions of the chemical potential, demonstrating that they are much less sensitive to the matrix elements than the peak sizes and that they are mainly fixed by the vortex fluctuation frequency, which might be much larger than the other energy scales of the problem.

Simplifying the self-energy and plugging into (C6) shows that independent of chemical potential for $l = 0$ we have

$$\Delta\omega_0^\sigma\left[\left(\Delta\omega_0^\sigma\right)^2 - (\delta + \omega_c/2 + \omega_v)^2 + \left(A_{0;1}^{\sigma;+} + A_{-1;0}^{\sigma;+}\right)\right]$$

$$+ (\omega_v + \delta + \omega_c/2)\left(A_{0;1}^{\sigma;+} - A_{-1;0}^{\sigma;+}\right) = 0. \tag{C9}$$

Using $A_{0;1}^{\sigma;+} \approx A_{-1;0}^{\sigma;+}$ we get results similar to Ref. [17] for an ordinary s-wave superconductor. Since the matrix elements are much smaller than the other parameters, we can neglect them in above equation. We then get

$$\Delta\omega_0^\sigma\left[\left(\Delta\omega_0^\sigma\right)^2 - (\delta + \omega_c/2 + \omega_v)^2\right] = 0 \tag{C10}$$

for any μ. This gives a central and two satellite peaks at, respectively,

$$\Delta\omega_0^\sigma = 0, \tag{C11}$$

$$\Delta\omega_0^\sigma = (\omega_v + \delta + \omega_c/2), \tag{C12}$$

$$\Delta\omega_0^\sigma = -(\omega_v + \delta + \omega_c/2). \tag{C13}$$

For $l = 1$, we may as well neglect the contributions from the matrix elements. For $\mu < \bar{\mu}_-$,

$$\Delta\omega_1^-[(\Delta\omega_1^- - \omega_v)^2 - (\delta + \omega_c/2)^2] = 0, \tag{C14}$$

$$\Delta\omega_1^+[(\Delta\omega_1^+)^2 - (\omega_v + \delta + \omega_c/2)^2] = 0. \tag{C15}$$

So we have peaks at

$$\Delta\omega_1^- = 0, \tag{C16}$$

$$\Delta\omega_1^- = \omega_v + (\delta + \omega_c/2), \tag{C17}$$

$$\Delta\omega_1^- = \omega_v - (\delta + \omega_c/2), \tag{C18}$$

and

$$\Delta\omega_1^+ = 0, \tag{C19}$$

$$\Delta\omega_1^+ = (\omega_v + \delta + \omega_c/2), \tag{C20}$$

$$\Delta\omega_1^+ = -(\omega_v + \delta + \omega_c/2). \tag{C21}$$

For $\mu > \bar{\mu}_+$ the roles of $+$ and $-$ in the above equations are exchanged. Since the total density is the sum of contributions from both $\sigma = \pm$ sectors and the gap between E_1^+ and E_1^- goes as $\delta(1/2 - \phi/2\pi)$, the LDOS in the two regimes of $\mu < \bar{\mu}_-$ and $\mu > \bar{\mu}_+$ look the same.

We now get to the most important regime of $\bar{\mu}_- < \mu < \bar{\mu}_+$. The positions of the peaks for both $\sigma = \pm$ sectors are at

$$\Delta\omega_1^\sigma = 0, \tag{C22}$$

$$\Delta\omega_1^\sigma = (\omega_v + \delta + \omega_c/2), \tag{C23}$$

$$\Delta\omega_1^\sigma = -(\omega_v + \delta + \omega_c/2). \tag{C24}$$

Clearly, as μ crossed $\bar{\mu}_-$ the third peak for the $\sigma = -$ sector is shifted by $-2\omega_v$, and this leads to a clear modification of the LDOS which persists up the $\mu = \bar{\mu}_+$ at which the peak from

the $\sigma = +$ sector moves by $2\omega_v$ and recovers the original LDOS.

The creation of a satellite peak at positive energy should not happen without an accompanying compensation of a positive energy peak jumping into negative energies. Indeed, such a compensation does occur for the contribution of $l = -1$ (which exchanging angular momentum with the vortex motion is connected to $l = -2$ and $l = 0$, the latter giving the jump). It just turns out that, since the spatial dependence of the LDOS is determined by $u_l^\sigma(\mathbf{r})$ as can be seen from (C4), the peaks from $l = -1$ do not contribute to the LDOS at the center of the vortex $r = 0$. The peaks from $l = -1$ should contribute to the LDOS at a distance of $\sim k_F^{-1}$ from the vortex center, which should be on the order of 10 Å in a superconducting TI. This can be resolved with the current STM technology.

[1] X. G. Wen, Int. J. Mod. Phys. B **04**, 239 (1990).
[2] M. A. Levin and X.-G. Wen, Phys. Rev. B **71**, 045110 (2005).
[3] F. Burnell and S. H. Simon, Ann. Phys. **325**, 2550 (2010).
[4] F. Wilczek, Nat. Phys. **5**, 614 (2009).
[5] V. Mourik, K. Zuo, S. M. Frolov, S. R. Plissard, E. P. A. M. Bakkers, and L. P. Kouwenhoven, Science **336**, 1003 (2012).
[6] S. Nadj-Perge, I. K. Drozdov, J. Li, H. Chen, S. Jeon, J. Seo, A. H. MacDonald, B. A. Bernevig, and A. Yazdani, Science **346**, 602 (2014).
[7] B. A. Bernevig, T. L. Hughes, and S.-C. Zhang, Science **314**, 1757 (2006).
[8] R. M. Lutchyn, J. D. Sau, and S. Das Sarma, Phys. Rev. Lett. **105**, 077001 (2010).
[9] P. Ghaemi, S. Gopalakrishnan, and T. L. Hughes, Phys. Rev. B **86**, 201406 (2012).
[10] P. Ao and D. J. Thouless, Phys. Rev. Lett. **70**, 2158 (1993).
[11] P. G. De Gennes and J. Matricon, Rev. Mod. Phys. **36**, 45 (1964).
[12] J. Bardeen and M. J. Stephen, Phys. Rev. **140**, A1197 (1965).
[13] C. Caroli, P. G. De Gennes, and J. Matricon, Phys. Lett. **9**, 307 (1964).
[14] H. F. Hess, R. B. Robinson, and J. V. Waszczak, Phys. Rev. Lett. **64**, 2711 (1990).
[15] A. Maldonado, S. Vieira, and H. Suderow, Phys. Rev. B **88**, 064518 (2013).
[16] C. J. Chen, in *Introduction to Scanning Tunneling Microscopy*, edited by M. Lapp, J.-I. Nishizawa, B. B. Snavely, H. Stark, A. C. Tam, and T. Wilson, Oxford Series in Optical and Imaging Sciences (Oxford University Press, New York, 1993).
[17] L. Bartosch and S. Sachdev, Phys. Rev. B **74**, 144515 (2006).
[18] P. Nikolić and S. Sachdev, Phys. Rev. B **73**, 134511 (2006).
[19] P. Nikolić, S. Sachdev, and L. Bartosch, Phys. Rev. B **74**, 144516 (2006).

[20] Y. S. Hor, A. J. Williams, J. G. Checkelsky, P. Roushan, J. Seo, Q. Xu, H. W. Zandbergen, A. Yazdani, N. P. Ong, and R. J. Cava, Phys. Rev. Lett. **104**, 057001 (2010).
[21] L. A. Wray, S.-Y. Xu, Y. Xia, Y. S. Hor, D. Qian, A. V. Fedorov, H. Lin, A. Bansil, R. J. Cava, and M. Z. Hasan, Nat. Phys. **6**, 855 (2010).
[22] T. V. Bay, T. Naka, Y. K. Huang, H. Luigjes, M. S. Golden, and A. de Visser, Phys. Rev. Lett. **108**, 057001 (2012).
[23] S. Sasaki, M. Kriener, K. Segawa, K. Yada, Y. Tanaka, M. Sato, and Y. Ando, Phys. Rev. Lett. **107**, 217001 (2011).
[24] L. Fu and E. Berg, Phys. Rev. Lett. **105**, 097001 (2010).
[25] L. Fu and C. L. Kane, Phys. Rev. Lett. **100**, 096407 (2008).
[26] P. Hosur, P. Ghaemi, R. S. K. Mong, and A. Vishwanath, Phys. Rev. Lett. **107**, 097001 (2011).
[27] C.-K. Chiu, P. Ghaemi, and T. L. Hughes, Phys. Rev. Lett. **109**, 237009 (2012).
[28] H.-H. Hung, P. Ghaemi, T. L. Hughes, and M. J. Gilbert, Phys. Rev. B **87**, 035401 (2013).
[29] A. Y. Kitaev, Phys.-Usp. **44**, 131 (2001).
[30] H. Zhang, C.-X. Liu, X.-L. Qi, X. Dai, Z. Fang, and S.-C. Zhang, Nat. Phys. **5**, 438 (2009).
[31] F. Gygi and M. Schlüter, Phys. Rev. B **43**, 7609 (1991).
[32] L. Hedin, Phys. Rev. **139**, A796 (1965).
[33] E. Gaidamauskas, J. Paaske, and K. Flensberg, Phys. Rev. Lett. **112**, 126402 (2014).
[34] R. Wakatsuki, M. Ezawa, and N. Nagaosa, Phys. Rev. B **89**, 174514 (2014).
[35] L. Bartosch, L. Balents, and S. Sachdev, Ann. Phys. (N.Y.) **321**, 1528 (2006).
[36] Y. S. Hor, Y. Qiu, K. N. Sanders, J. E. Medvedeva, T. Vojta, J. Dai, W. Wu, and P. Ghaemi, http://meetings.aps.org/link/BAPS.2015.MAR.M12.1
[37] J. E. Sonier, J. Phys.: Condens. Matter **16**, S4499 (2004).